Research article

Investigations on anticancer activity of Eu^{3+} doped hydroxyapatite nanocomposites against MCF7 and 4T1 breast cancer cell lines: A structural and luminescence Perspective

K Sai Manogna [a], B Deva Prasad Raju [b], G Rajasekhara Reddy [c], Parashuram Kallem [d,**], Mannur Ismail Shaik [e,***], N John Sushma [a,*]

[a] *Department of Biotechnology, Sri Padmavati Mahila Visvavidyalayam, (Women's University) Tirupati-517 502, India*
[b] *Department of Physics, Sri Venkateswara University, Tirupati - 517501, India*
[c] *School of Mechanical Engineering, Yeungnam University, Gyeongsan, 38541, Republic of Korea*
[d] *Environmental Health and Safety Program, College of Health Sciences, Abu Dhabi University, Abu Dhabi, United Arab Emirates*
[e] *Faculty of Fisheries and Food Science, University Malaysia Terengganu, KulaNerus-21030, Terengganu, Malaysia*

ARTICLE INFO

ABSTRACT

Breast cancer remains a significant global health concern, necessitating the development of novel therapeutic approaches. In this study, we investigate the role of Eu^{3+} doped hydroxyapatite nanocomposites (Han: Eu^{3+}) in the treatment of MCF7 and 4T1 breast cancer cell lines. Furthermore, we explored the structural and luminescent properties of these nanocomposites. Han: Eu^{3+} were synthesized using a modified co-precipitation method, and their morphology and crystal structure were characterized using scanning electron microscopy (SEM) and X-ray diffraction (XRD) in which the average crystalline size of Han: Eu^{3+} was found to be 25 nm, rendering them suitable for cellular uptake and targeted therapy. To gain insights into the luminescent properties of Han: Eu^{3+}, their excitation and emission spectra were recorded using photoluminescence spectrometer. The characteristic red emission of Eu^{3+} ions was observed upon excitation, validating the successful doping of Eu^{3+} into the Han lattice, which was confirmed by the CIE chromaticity coordinate study. These luminescent properties of Han: Eu^{3+} hold promise for potential applications in bioimaging. To evaluate the efficacy of Han: Eu^{3+} in breast cancer treatment, MCF7 and 4T1 cell lines were exposed to varying concentrations of the nanocomposites. Cell viability assays revealed a concentration-dependent reduction in cell viability, indicating the potential anticancer activity of Han: Eu^{3+}. The findings of this study contribute to the expanding field of nanomedicine, bringing targeted breast cancer treatments and us closer to more effective.

* Corresponding author.
** Corresponding author.
*** Corresponding author.
E-mail addresses: parashuram.kallem@adu.ac.ae (P. Kallem), mannurismail@umt.edu.my (M.I. Shaik), johnsushma@gmail.com (N. John Sushma).

1. Introduction

Enhanced permeation and retention (EPR) effect-mediated selective accumulation of nanoparticles in cancer tissue has made them a promising tool for cancer diagnosis and treatment [1]. Breast cancer is the most commonly diagnosed cancer in women globally, representing 25 % of all cancer cases. This malignancy is the most common cancer in both genders and holds the top position as the primary cause of mortality resulting from cancer in females. According to estimates, breast cancer accounted for one in every eight newly diagnosed cases of cancer in the year 2020, with a total of approximately 2.3 million cases reported. According to recent statistics, breast cancer accounted for approximately 684,996 fatalities in 2020, with a significant proportion of these deaths concentrated in regions with limited access to resources [2]. Typically, neoplastic cells of breast cancer aggregate to form a mass frequently detectable through radiographic imaging or palpation as a discrete nodule. In cases where breast cancer metastasizes beyond the primary site and infiltrates the bloodstream and lymphatic system, it progresses to an advanced stage. *Metastatic breast cancer* is the term used to describe the spread of breast cancer to other organs, including but not limited to the liver, lungs, bones, and brain. The time at which the ailment is identified represents a significant prognostic indicator. According to research, a significant proportion of patients diagnosed and treated for a localized primary breast cancer tumour have a survival rate of over five years, reaching up to 99 % [3]. The survival rate of patients with metastatic disease significantly declines, with a mere 23 % of individuals surviving beyond five years [4]. The treatment modalities available for metastases are often constrained [5]. The efficacy of surgery in managing localized primary tumors is well-established. However, its utility in resecting multiple metastatic lesions is limited. This is supported by existing literature [6]. The efficacy of medication may be compromised if the administered doses, whether orally or intravenously, do not adequately reach the intended sites, as per sources [7,8]. Targeted therapies and immunotherapies represent a novel and auspicious approach to managing breast cancer [9,10]. Drug repurposing is gaining significant traction as a means to expedite the drug development process. This is because the safety and efficacy of existing approved drugs have already been established, resulting in a reduction in attrition rate, timestamp, and cost from bench to pilot compared to new drug development [11].

In cancer drug development, the conventional approach involves the initial stages of lead identification and optimization, followed by pre-clinical and clinical studies to ascertain the drug's safety, toxicity, and effectiveness as an anti-cancer agent. Currently, many clinical trials are recorded on the clinical trial website [12]. Celecoxib has exhibited significant potential in inhibiting the metastasis and proliferation of tumour cells through its targeting of COX-2, regulation of the tumour microenvironment, and sensitization of cancer cells to other treatments. This represents a promising avenue for drug treatments in this area [13–16]. The therapeutic agent Fluorouracil (5-FU) has been sanctioned for treating breast cancer. Its anti-cancer properties are attributed to its ability to impede cancer progression, trigger apoptosis, and reduce metastasis. These effects are achieved through various mechanisms, including inhibiting the Ras/ERK pathway, downregulating the NF-κB gene expression, and enhancing therapeutic efficacy when used with targeted nanoparticle-based therapies [17–21]. Metformin, a commonly prescribed medication for diabetes, exhibits anti-cancer properties in breast cancer through its interaction with AMPK, inhibition of various signaling pathways, reduction of inflammation, and potential for combination therapy. These attributes position it as a promising contender for treating breast cancer [22–26]. Nitroxoline, initially utilized as an antibiotic for treating urinary tract infections, has demonstrated considerable efficacy in combating cancer. It has been observed to possess anti-cancer properties such as anti-angiogenic activity and the ability to impede tumour growth, metastasis, and invasion in diverse forms of cancer. These attributes make it a promising therapeutic option for treating breast cancer, with the added advantage of a favorable pharmacokinetic profile and minimal toxicity [27,28]. Penfluridol, initially developed as an antipsychotic medication, has exhibited significant anti-tumour properties in multiple cancer cell lines and in vivo models, including breast cancer. These effects are attributed to various mechanisms, such as inhibiting integrin signaling, induction of apoptosis and autophagy, suppressing metastasis, disruption of mitochondrial and lysosomal functions, and inhibition of angiogenesis. As a result, it has the potential to be a promising candidate for the treatment of breast cancer, with enduring effects and the possibility of being used in combination therapies [29–32]. Tamoxifen (TAM) is a selective oestrogen receptor modulator (SERM) commonly employed as a therapeutic intervention for breast cancer patients with oestrogen receptor-positive tumors. Its mechanism of action involves inhibiting oestrogen receptor (ER) signaling, which leads to cell cycle arrest and decreased proliferation. In addition to its anti-cancer effects, TAM has been shown to provide other benefits, such as reducing the risk of recurrence, improving disease-free survival, and enhancing outcomes in specific patient subgroups. As a result, TAM is considered to be a highly efficacious treatment option for breast cancer [33–36]. Doxorubicin (ADM) is an anthracycline antibiotic with strong antineoplastic properties and is effective against several types of cancer, including breast cancer. Its therapeutic mechanism involves DNA intercalation, Topo-II disruption, ROS generation, and induction of apoptosis. However, using liposomal formulations, such as PEGylated liposomal doxorubicin (PLD), in combination therapies has been shown to enhance its efficacy while reducing cardiotoxicity, as reported in previous studies [37–39].

Luminous nanoparticles exhibit exceptional potential as optical probes for medical and biological imaging applications. The primary role of these entities is to furnish the essential fluorescence contrast that is imperative for visualizing particular cellular constituents and tissues [40]. Various luminescent materials, such as gold nanoparticles [41], quantum dots [42], monoclonal antibodies [43], nanodiamonds [44], nanostructures labelled with organic dyes [45], and rare earth-doped nanomaterials [46] have been suggested as potential fluorophores for applications in biosensing and bioimaging. Lanthanide-doped nanoparticles have been recognized as a new classification of probes that exhibit a prolonged fluorescence lifetime, elevated quantum yield, distinct emission peaks, colour modulation based on the lanthanide ion-doped, and exceptional resilience to photo-bleaching instigated by environmental factors. The utilization of hydroxyapatite (HA) nanoparticles as nanoplatforms for the effective doping of lanthanides is significant in this context. The primary component of natural bone mineral is Hydroxyapatite (HA), which possesses noteworthy attributes, including facile functionalization, biocompatibility, bioactivity, and efficient biodegradability in biological settings [47,48]. The biocompatibility of hydroxyapatite nanocomposites makes them appropriate for use in biomedical applications due to their numerous physiological

interfaces and physicochemical properties at the nanoscale. The terms "tissue revamp" and "recovery" are frequently utilized interchangeably, particularly in the domain of injury rehabilitation [49].

Europium has garnered considerable interest in bioimaging due to its distinctive spectroscopic characteristics, which include high quantum yield, narrow emission bands, and long fluorescence lifetime. The aforementioned characteristics render it a highly suitable contender for employment in bioimaging endeavours, particularly in fluorescence microscopy [50] and magnetic resonance imaging (MRI) [51]. Furthermore, the utilization of europium complexes as probes for identifying and measuring diverse biomolecules, including proteins, DNA, and enzymes, has been documented [52].

In the present context, the escalating cost of oncological drugs that have received marketing approval has exacerbated the financial burden rather than alleviation it. Consequently, exploring an alternative methodology that can effectively address the challenges of escalating attrition rate, time, and cost in the cancer drug development process is imperative. The objective of the current research was to thoroughly examine the feasibility of synthesizing luminescent biomimetic and highly biocompatible Eu-doped hydroxyapatite nanocomposites through the precipitation method under controlled conditions. Additionally, the study aimed to investigate these nanocomposites physicochemical and cytocompatibility properties. In this study, we conducted measurements of the sensitized fluorescence of Eu (III) to investigate its luminescence properties. Initially, the precipitates of Eu-doped hydroxyapatite (Han: Eu^{3+} NCs) nanocomposites (NCs) were generated by the precipitation of solutions containing Eu^{3+}/Ca^{2+}/Chloride/Citrate/Phosphate. Subsequently, a comprehensive characterization of the aforementioned precipitates was performed using a diverse range of complementary techniques. Particular emphasis was placed on identifying the circumstances that facilitate the acquisition of biomimetic characteristics. The sensitized fluorescence was measured to investigate the luminescence properties of the generated particles. Subsequently, the cytocompatibility of said particles was evaluated through In vitro cellular assays.

2. Materials and methods

2.1. Reagents

The chemicals Calcium chloride, Ammonium dihydrogen phosphate, Sodium dihydrogen phosphate and disodium hydrogen phosphate were from Merck (Bangalore, India). Europium oxide was obtained from Sigma (Sigma Aldrich, Bangalore, India). Sodium dihydrogen phosphate and disodium hydrogen phosphate obtained from Merck chemicals were utilized for buffer preparations. Doxorubicin, MCF7 and 4T1 breast cancer cell lines were used for *in vitro* studies.

2.2. Methodology

Preparation of Europium Chloride: Europium oxide was converted to europium chloride by dissolving with hydrochloric acid which then followed by evaporation of the solvent.

2.3. Synthesis of nanocomposites

In the synthesis process, 7.315 g of 1 M Calcium chloride ($CaCl_2$) was dissolved in 50 ml of distilled water. 5.75 g of 1 M Sodium dihydrogen phosphate ($Na_2H_2PO_4$) was dissolved in 50 ml of distilled water. The solution of Calcium chloride and Ammonium dihydrogen phosphate were mixed. The as synthesized Calcium chloride and Ammonium dihydrogen phosphate solution herein after been abbreviated as Han (Hydroxyapatite Nanocomposites). To this Han solution 0.5 g of Europium chloride was added as dopant. Since the prepared solution is in acidic medium, the authors added ammonium hydroxide and Sodium hydroxide solution to make it alkaline pH i.e., approximately 8. The resultant opaque colloidal mixture underwent filtration, multiple rinses with an aqueous solution, and subsequent separation by decantation. Ultimately, the suspension underwent centrifugation. After that the pellet obtained had to be dried completely and macerated with mortar and pestle. The resultant finely powdered nanocomposite consists of Han: Eu^{3+}. The nanocomposites that were synthesized henceforth denoted as Han: Eu^{3+} NCs in the subsequent examinations.

2.4. Particle characterizations

Different characterization techniques were used for the nanocomposites, including, X-Ray Diffraction Spectroscopy (XRD), X-ray Photoelectron Spectroscopy (XPS), Differential Scanning Calorimetry (DSC), Fourier Transform Infrared Spectroscopy (FTIR), Scanning Electron Microscopy and Energy Dispersive X-Ray Spectroscopy (SEM-EDS), Photoluminescence (PL) studies, Particle size and *In vitro* cytotoxicity tests.

2.4.1. Fourier Transform Infrared Spectroscopy
Fourier transform infrared spectra were initially recorded with a Bruker Alpha II FTIR spectrometer equipped with an attenuated total reflectance (ATR) accessory of Zinc-selenium crystal. The prepared powdered samples were directly placed on the crystal and were recorded within the wave number range from 4000 cm^{-1} to 500 cm^{-1}.

2.4.2. X-Ray Diffraction Spectroscopy (XRD)
The X-ray diffraction (XRD) data were obtained using the AERIS PAN analytical diffractometer with para focusing geometry and Cu Kα1 radiation (1.5406 Å). The homogeneously dispersed powdered specimens were applied onto the sample plate and subsequently

positioned onto the holder for analytical purposes. The high-score software was utilized for conducting data processing.

2.4.3. X-ray Photoelectron Spectroscopy (XPS)

The elemental composition and oxidation states of the specimen were ascertained by utilizing an X-ray Photoelectron Spectrometer (XPS). The analysis was conducted using the K-alpha model provided by Thermo Scientific, a company based in the United States. The XPS system employed in this study utilizes monochromatic Al Kα X-ray radiation, characterized by a source energy of 1486.6 eV. This specific energy facilitates accurately determining binding energies corresponding to various elements in the analyzed sample. Data was acquired and processed using the Avantage commercial software (version 5.932, Thermo Scientific, USA). The XPS data was recorded, and initial processing steps, such as background correction and noise reduction, were performed using comprehensive software.

2.4.4. Scanning electron microscopy (SEM-EDAX)

The CHN analysis, encompassing carbon, hydrogen, and nitrogen elements, was conducted utilizing the PerkinElmer 2400 CHN elemental analyzer (PerkinElmer). Additionally, the EDAX analysis was performed on the EDAX APEX. The solubility profile of the Han: Eu^{3+} specimen indicates its solubility in water and partial solubility in DMSO, methanol, chloroform, acetonitrile, and ethanol while exhibiting insolubility in diethyl ether.

2.4.5. Differential Scanning Calorimetry

The thermal characteristics of Han: Eu^{3+} produced synthetically were examined using a TA 2920 modulated DSC thermal analyzer (TA Instruments, New Castle, DE). The analysis was performed on a calcinated sample weighing approximately 10 mg and placed in an aluminium pan. A protective atmosphere comprising Nitrogen (N_2) gas was employed, with a gas flow rate of 50 mL/min. The pan was subjected to a hermetic seal and subsequently underwent a temperature increase from 50 °C to 300 °C at 10 °C per minute. The thermodynamic properties of the sample were determined using the Universal Analysis Programme, Version 1.9 D. These properties include the onset temperature (Tm), denaturation temperature (Td), enthalpy of denaturation (ΔH), and cooperativity, which is represented by the width at half-peak height (ΔT1/2).

2.4.6. Photoluminescence studies

The present study examined the excitation and emission properties of Han: Eu^{3+} NCs. This investigation was conducted using an FLS-1000 spectrofluorometer equipped with PMK 980 and PMT 1700 detectors. The preparation of the nanocomposites suspension was conducted. Subsequently, it was introduced into a quartz cuvette in order to mitigate any potential interference that could arise during the measurement process. An emission analysis was conducted using the PMT 1700 detector, encompassing wavelengths ranging from 950 nm to 1650 nm. A set of emission spectra was documented under the condition of a consistent excitation wavelength. The excitation analysis was conducted by systematically varying the excitation wavelength from 230 to 980 nm while keeping the emission wavelength constant. The emission intensity was measured and graphed as a function of the excitation wavelength to generate excitation spectra, which offer insights into the energy levels and electronic transitions associated with the excitation phenomenon.

2.5. In vitro studies

The MCF7 cell line, a human breast cancer cell line, was procured from NCCS, Pune, India. Additionally, the 4T1 cell line, a mouse breast cancer cell line, was obtained from ATCC, United States. The MCF7 cells were cultured in DMEM high glucose medium, while the 4T1 cells were cultured in RPMI-1640 medium. Both cell lines were cultured in an atmosphere containing 5 % CO_2 and 18–20 % O_2 at 37 °C in a CO_2 incubator. The culture medium was supplemented with 10 % FBS and a 1 % antibiotic-antimycotic solution. The cells were sub-cultured every 2–3 days. The present study utilized passages 59 and 24, respectively and further MTT assay was performed.

2.5.1. MTT assay

The experimental procedure involved seeding a 96-well plate with 200 μl cell suspension at 20,000 cells per good density. The cells were then allowed to grow for 24 h without the test agent. The drug concentrations table was referenced to ensure that the wells were treated with the correct concentrations of the test agents. Subsequently, the plate was incubated for 24 h at 37 °C in an atmosphere containing 5 % CO_2. Following the incubation period, the residual media was extracted and supplemented with MTT reagent at a concentration of 0.5 mg/mL in the entire solution. The plate was enveloped with aluminium foil to prevent photo damage and subsequently placed back into the incubator for 3 h. Subsequently, the MTT reagent was eliminated, and a solubilization solution (DMSO) was introduced into each well. To improve dissolution, a gyratory shaker was employed for gentle stirring, while periodic pipetting up and down was carried out to ensure complete dissolution of MTT formazan crystals, especially in cultures with high cell density. Subsequently, absorbance was measured using either a spectrophotometer or an ELISA reader, with a wavelength of 570 nm.

% Cell viability is calculated using below formula:

% Cell viability = [Mean abs of treated cells/Mean abs of Untreated cells] x 100.

The IC_{50} value was determined by using linear regression equation i.e., $\mathbf{Y = mx + C.}$

Here, Y = 50, M and C values were derived from the viability graph.

3. Results and discussion

3.1. Fourier Transform Infrared Spectroscopy

The peak found at 1017 cm^{-1} shows the C–O stretch. Another peak found at 1396 cm^{-1} represents the O–H bending and the peak found at 1594 cm^{-1} possibly shows the presence of N–H bending. The results were shown in Table 1 and Fig. 1.

3.2. X-ray diffraction analysis

The X-Ray Diffraction analysis was done for Han: Eu^{3+} NCs with CuKα radiation in the 2θ range 10°–90°. Fig. 2 represents the XRD spectrum of Han: Eu^{3+} NCs. The crystalline size was calculated using Scherer's equation. The average crystalline size of the Han: Eu^{3+} NCs is 25 nm as depicted in Table 2.

3.3. X-ray Photoelectron Spectroscopy (XPS)

The X-ray Photoelectron Spectroscopy (XPS) survey spectrum analysis of Europium (Eu^{3+}) doped Hydroxyapatite Nanocomposites (Han: Eu^{3+} NCs) has provided valuable insights into their elemental composition and chemical environment, which are crucial for understanding their potential role in the treatment of breast cancer cell lines MCF7 and 4T1, as well as their structural and luminescence properties for cancer diagnostics. A series of scans were performed for different elements and peaks, and the data obtained is presented in Table 3.

The main peak observed at 1134.04 eV in Fig. 3(a–h) corresponds to the Eu^{3+} 3d$_{5/2}$ photoelectron peak, confirming the presence of (Eu^{3+}) in the sample. This observation is significant in the context of cancer therapeutics, as Eu^{3+} ions are known for their luminescent properties, and their presence could offer potential benefits for cancer imaging and tracking of nanocomposites delivery in live cells. However, the atomic percentages for Europium are not provided, hindering a comprehensive understanding of its concentration.

The XPS analysis revealed the presence of Oxygen (O), Sodium (Na), Carbon (C), Calcium (Ca), Phosphorus (P), and Chlorine (Cl) on the surface of the Europium (Eu^{3+}) metal sample. The presence of multiple phosphorus (P) peaks in Fig. 3(g) corresponds to the 2p region with distinct binding energies (131.88 eV and 132.78 eV) suggests the existence of different chemical environments for phosphorus atoms on the nanocomposites surface. This diversity in phosphorus species could be attributed to different phosphorus-containing functional groups, which might play a crucial role in the interaction between Han: Eu^{3+} NCs and cancer cells. Additionally, the presence of an extra peak at 135.18 eV (P 2p - o) may indicate a unique phosphorus species, which warrants further investigation to understand its potential implications for cancer treatment. The detection of chlorine (Cl) peaks in Fig. 3(f) at specific binding energies indicates the possible incorporation of chlorine in the Han: Eu^{3+} NCs. Chlorine is not a common component in hydroxyapatite, and its presence related to the synthesis process or interactions with the surrounding environment. Understanding the role of chlorine in the context of cancer cells is essential, as it influence the cellular uptake, biodistribution, and toxicity of the nanocomposites. The observation of multiple carbon (C) peaks in Fig. 3(e) corresponds to the 1s region suggests the presence of diverse carbon-containing functional groups on the nanocomposites surface. These organic moieties may stem from the capping agents or stabilizers used during nanocomposite synthesis or from adsorbed biomolecules. The abundant presence of carbon-based functional groups may have implications for the surface chemistry and biological interactions of Han: Eu^{3+} NCs with cancer cells.

Calcium (Ca) peaks were clearly identified in Fig. 3(d), confirming the presence of calcium in the Han: Eu^{3+} NCs. Calcium is an integral component of hydroxyapatite, and its presence is crucial for maintaining the nanocomposite's structural integrity and stability. Calcium ions have been implicated in cellular signaling and apoptosis pathways in cancer cells, and their presence on the nanocomposite surface could influence cellular responses and therapeutic outcomes. The observation of multiple oxygen (O) peaks in Fig. 3(c) corresponds to the 1s region indicates the existence of diverse oxygen-containing functional groups on the nanocomposite surface. Oxygen plays a vital role in hydroxyapatite's biocompatibility and bioactivity, and its presence in abundance on the Han: Eu^{3+} NCs is expected to be advantageous for cellular interactions and potential therapeutic effects in cancer cells. Finally, the detection of sodium (Na) peaks in Fig. 3(b) suggests the presence of sodium on the nanocomposite surface. Sodium ions have important roles in cellular homeostasis and transport mechanisms, and their presence in the Han: Eu^{3+} NCs could have implications for cellular uptake and internalization.

For instance, the higher areas under the O1s and C1s peaks suggest a relatively higher abundance of Oxygen and Carbon on the sample surface compared to other elements. The XPS survey spectrum analysis of Han: Eu^{3+} NCs provides crucial insights into their surface chemistry and elemental composition. Understanding the specific functional groups and elements present on the nanocomposite surface is essential for tailoring their properties for cancer therapeutics and diagnostics. The presence of diverse chemical species, such as phosphorus, chlorine, calcium, oxygen, carbon, and sodium, indicates a complex and heterogeneous surface

Table 1
Comparison of Experimental and Literature frequencies with their Band assignments.

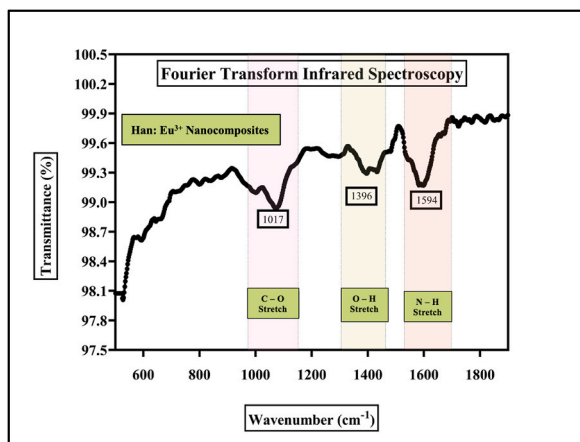| Experimental Frequencies [Wavenumber (cm^{-1})]	Literature Frequencies	Band Assignment
1017 cm^{-1}	1400–1000	C – O Stretch
1396 cm^{-1}	1310–1400	O – H Bending
1594 cm^{-1}	1650–1580	N – H Bending

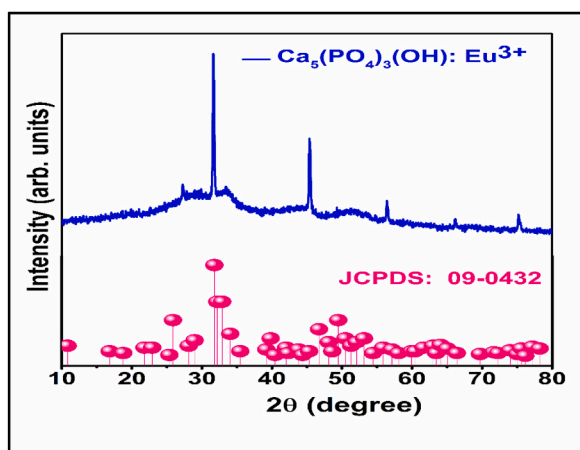**Fig. 1.** FTIR spectrum of Han: Eu^{3+} nanocomposites.

Fig. 2. XRD spectrum of Han: Eu^{3+} NCs.

Table 2
The X-ray Diffraction peak positions, its corresponding full width half Maxima and crystalline size of Han: Eu^{3+} NCs.

Peak Position (2 Theta)	FWHM	Crystalline Size (nm)
27.29	0.286	26.993
31.66	0.2433	31.413
45.4	0.278	26.362
56.45	0.304	23.025
66.17	0.257	25.899
75.25	0.33	19.066
		Average: 25.460

composition that can be explored for targeted drug delivery, imaging, and theranostic applications. The results presented here lay the foundation for further investigations into the structural and luminescence properties of Han: Eu^{3+} NCs, ultimately paving the way for their potential use in the treatment of breast cancer cell lines MCF7 and 4T1, and other biomedical applications in cancer research.

3.4. Scanning electron microscopy (SEM-EDAX)

The crystalline nature of the particles present in the complexes has been verified through SEM analysis, which confirms their surface morphology. The morphology of particles in all complexes was examined through SEM micrograph analysis of Han: Eu^{3+} NCs, as depicted in Fig. 4, displays four distinct images (a-d) with varying magnifications, where (a) has a size of 10 μm, (b) 5 μm, (c) 2 μm,

Table 3
The table presents XPS data obtained from various scans, including the binding energies, full width at half maximum, areas under the peaks and atomic percentages of Han: Eu^{3+} NCs.

Name of the Element	Peak BE (eV)	FWHM eV	Area (P) CPS. eV	Atomic Percentage
Eu 3d$_{5/2}$	1134.04	3.73	53597.85	0
P 2p$_{3/2}$	131.88	1.32	2461.29	3.79
P 2p$_{1/2}$	132.78	1.32	1257.85	0
P 2p$_{P - o}$	135.18	3.07	1094.72	1.12
Cl 2p$_{3/2}$	197.96	1.74	2177.57	1.75
Cl 2p$_{1/2}$	199.53	1.74	1118.66	0
C 1s Peak 1	283.92	1.31	16162.5	24.44
C 1s Peak 2	287.55	1.27	6827.13	10.35
C 1s Peak 3	285.53	1.59	4301.53	6.51
Ca 2p$_{3/2}$	346.16	1.41	15631.77	6.24
Ca 2p$_{1/2}$	349.72	1.41	8050.45	0
O 1s Peak 1	530.17	1.55	43426.03	27.15
O 1s Peak 2	531.32	1.92	19109.26	11.96
O 1s Peak 3	534.94	1.57	1630.93	1.02
Na 1s Peak 1	1070.7	1.79	18255.79	5.66

BE: Binding Energy.
FWHM: Full Width at Half Maximum.
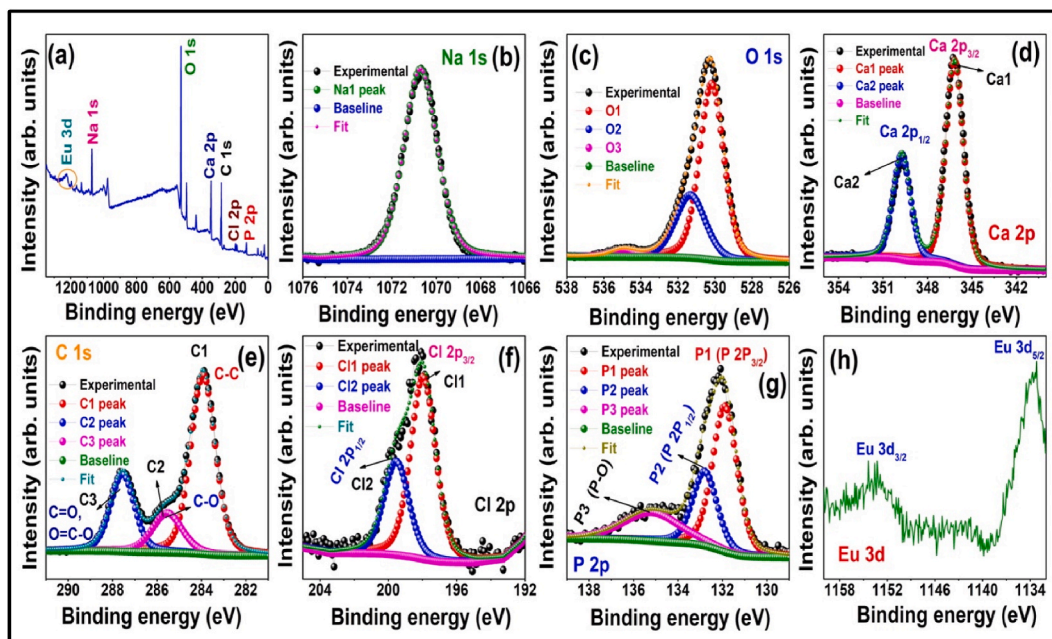Area (P) CPS.eV: Area under the peak.

Fig. 3. XPS spectrum (a) and (b–h) XPS core-level spectrum of individual elements of Han: Eu^{3+} NCs.

and (d) 1 μm, providing a comprehensive view of the specimens at different scales. The results indicate that the particles exhibit a crystalline structure, with some particles appearing aggregated. The elemental compositions of carbon, oxygen, chlorine, calcium, and europium present in the sample have been verified using EDAX analysis. The EDAX spectrum of Han: Eu^{3+} NCs (Fig. 5) demonstrates the congruity between the CHN and complexometric titration outcomes, as presented in Table 4, and provides compelling evidence that the molecular compositions of Han: Eu^{3+} NCs align with those of the synthesized sample.

3.5. Differential Scanning Calorimetry

The thermal gradient disparity between the specimen and the control may exhibit a positive or negative value. Heat is emitted during an exothermic process such as crystallization, resulting in a lower heat flow to the sample compared to the reference. In endothermic processes, such as melting, the heat flow is negative, indicating thermal energy transfer from the surrounding environment to the system. The DSC curve shows a shift of baseline at 60.81 °C indicating transition. Also, an endothermic peak is observed at 108.76 °C indicating an endothermic reaction caused by crystallization as depicted in Fig. 6.

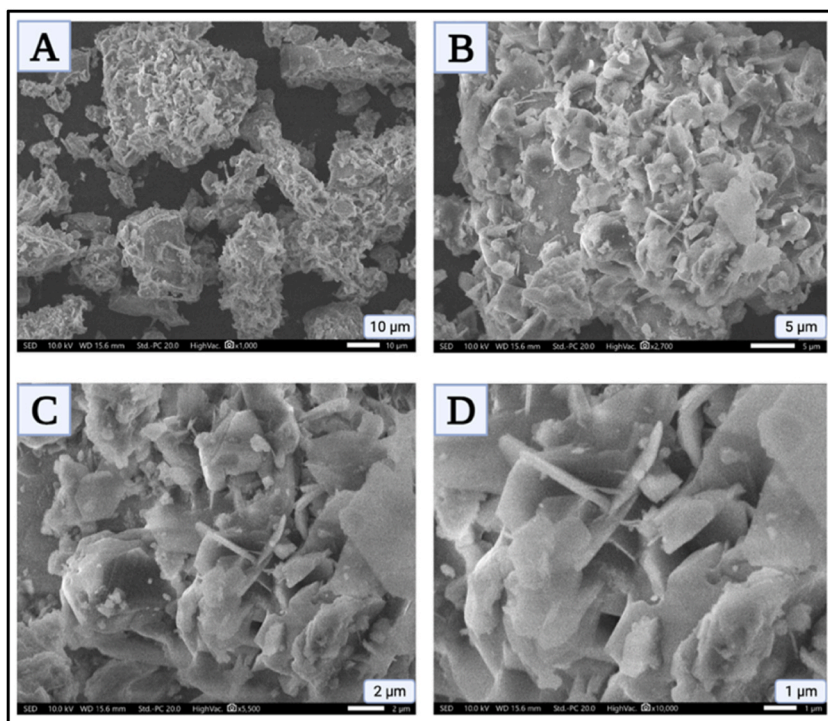**Fig. 4.** Scanning electron microscope image of Han: Eu^{3+} NCs confirming the crystalline nature of particles.
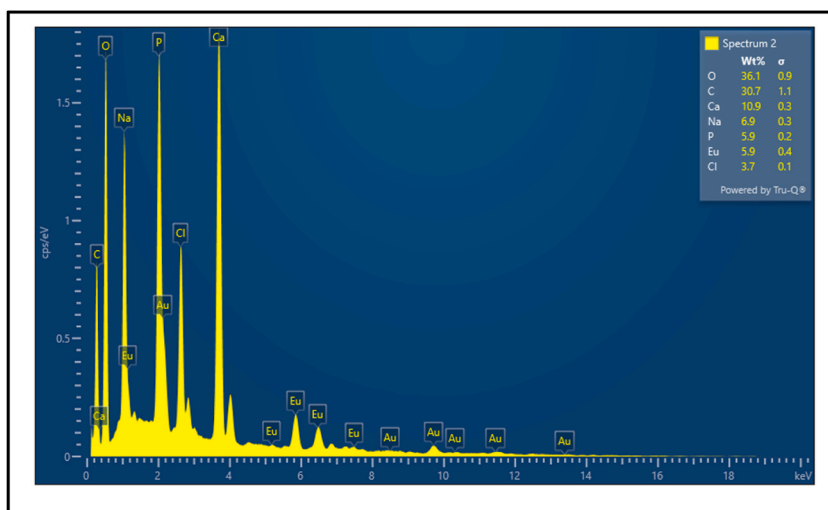

Fig. 5. Energy dispersive X-ray spectrum of Han: Eu^{3+} NCs.
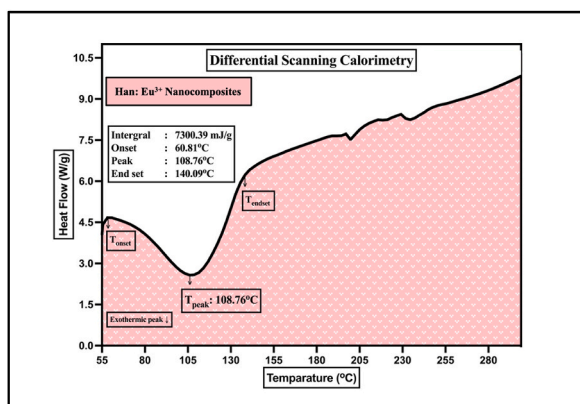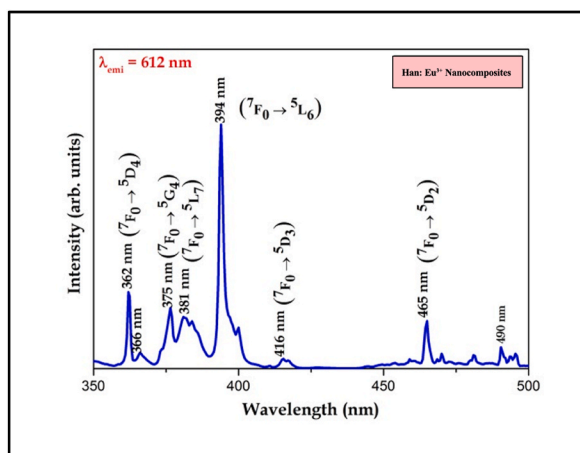
3.6. Excitation Spectrum

Fig. 7 shows the excitation spectrum of Han: Eu^{3+} NCs (monitoring emission at 612 nm). It shows multiple excitation peaks, the peak position and corresponding transition were shown in Table 5. Among all the peaks the peak at 394 nm has maximum intensity so, authors considered this 394 nm as an excitation wavelength for the Han: Eu^{3+} NCs.

3.7. Emission Spectrum

Fig. 8 shows the emission spectra of the Han: Eu^{3+} NCs under the excitation of 394 nm. It clearly shows emission peaks at 580 nm, (589 nm, 593 nm), 612 nm, 650 nm and 699 nm corresponding to the Eu^{3+} ions emission transitions such as $^5D_0 \rightarrow {}^7F_0$, $^5D_0 \rightarrow {}^7F_1$,

Table 4
Percentage analytical data of synthesized Han: Eu^{3+} NCs.

Element	Weight (% found)	Weight (% Sigma)	Atomic weight (% found)
C	30.68	1.13	44.70
O	36.12	0.86	39.50
Na	6.86	0.26	5.22
P	5.86	0.20	3.31
Cl	3.72	0.14	1.84
Ca	10.89	0.27	4.76
Eu	5.86	0.36	0.68

Fig. 6. DSC curve obtained on heating sample of Han: Eu^{3+} NCs (heating rate: 10 °C/min).

Fig. 7. The excitation spectrum of Han: Eu^{3+} NCs.

Table 5
Han: Eu^{3+} NCs excitation peak position and corresponding transitions.

S.No	Excitation peak Position (nm)	Transition
1	362	$^7F_0 \rightarrow {}^5D_4$
2	376	$^7F_0 \rightarrow {}^5G_4$,
3	382	$^7F_0 \rightarrow {}^5L_7$,
4	394	$^7F_0 \rightarrow {}^5L_6$,
5	414	$^7F_0 \rightarrow {}^5D_3$,
6	464	$^7F_0 \rightarrow {}^5D_2$,
7	524	$^7F_0 \rightarrow {}^5D_1$
8	534	$^7F_1 \rightarrow {}^5D_1$
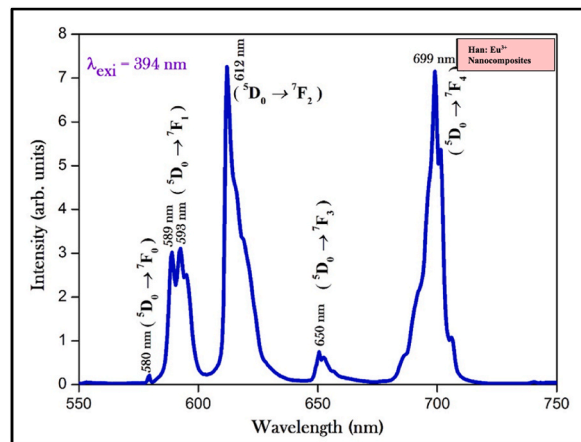
Fig. 8. Emission Spectrum of Han: Eu^{3+} NCs.

$^5D_0 \rightarrow {}^7F_2$, $^5D_0 \rightarrow {}^7F_3$ and $^5D_0 \rightarrow {}^7F_5$ respectively. The peaks corresponding to $^5D_0 \rightarrow {}^7F_2$ and $^5D_0 \rightarrow {}^7F_5$ are dominant and intensity of these two peaks is strongly dependent on the environment around the Eu^{3+} ions, both are hypersensitive in nature and the first one is hypersensitive, the latter is not [53,56]. So, it was clearly seen that the Han: Eu^{3+} NCs excited with 394 nm will emit radiation in the red region of the visible spectrum, and the same has been confirmed with CIE chromaticity coordinates in the next part. So, it is easy to identify the cancer tumors present in the cell lines of rats and human cell lines under UV light for which we gave treatment with Han: Eu^{3+} NCs.

3.8. CIE chromaticity coordinates

To determine the exact emission color of investigated Han: Eu^{3+} NCs sample using the emission data the authors adopted the procedure in the Commission International I'Eclaiage (CIE) france [54,55]. The CIE color coordinate and diagram were used to confirm the color of visible radiation. The authors were calculated CIE coordinates for Han: Eu^{3+} NCs (X = 0.643, Y = 0.355) and the CIE diagram which is shown in Fig. 9. From Fig. 9, it was clearly confirmed that the radiation emitted by the Han: Eu^{3+} NCs under 394 nm excitation were in the red region of the visible spectrum. The same was firmed in the previous section (emission analysis). So, it was strongly suggested that, Han: Eu^{3+} NCs in the cancer tumor will appear in red color under the UV (394 nm) excitation.

3.9. Lifetime analysis

The fluorescent lifetime decay analysis of Han: Eu^{3+} NCs was done with emission and excitations at 612 nm and 394 nm respectively, shown in Fig. 10. Decay profile is well fitted for exponential decay 2, authors were calculated lifetime for the excited level of Eu^{3+} ($^5D_0$) had been calculated ($\tau = 0.713$ ms). Eu^{3+} doped phosphors, which incorporate charge compensation, have the potential to serve as red-emitting phosphors for lamp applications. The material's luminescence performance is enhanced by charge compensation. Eu^{3+} doping in the Han lattice of Ca^{2+} is energetically more favorable due to the presence of charge compensator defects. The local symmetry around the Eu^{3+} ion disruption, resulting in the creation of deep states below the empty upper band, known as the
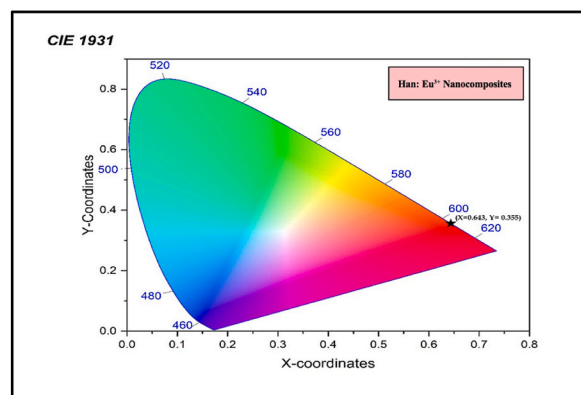

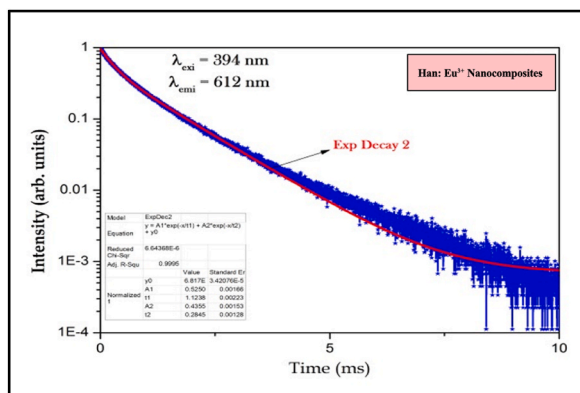**Fig. 9.** CIE chromaticity diagram of Han: Eu^{3+} NCs.

Fig. 10. Lifetime decay analysis of Han: Eu^{3+} NCs.

conduction band. Another study discusses the use of charge compensator defects in rare-earth-doped phosphors, evaluating three possible mechanisms and their impact on the electronic band structure to enhance the photoluminescence performance of the material for lamp applications [59]. These deep states can enhance intra-4f shell transitions, ultimately leading to an improvement in the emission intensity of Eu^{3+} doped hydroxyapatite nanocomposites.

3.10. Drug concentration details

In this study, the synthesized Han: Eu^{3+} NCs was evaluated to analyse the cytotoxicity effect on MCF7 cells. The concentrations of the test compounds as depicted in Table 6, were used to treat the cells.

3.10.1. Effect of Han: Eu^{3+} NCs on MCF7 cell lines

Fig. 11(a–f) and 12 demonstrates a dose-dependent analysis, revealing a discernible decrease in the number of cells as the concentration of Han: Eu^{3+} NCs increases. The concentrations examined (A: 6.25 µg/ml, B: 12.5 µg/ml, C: 25 µg/ml, D: 50 µg/ml, E: 100 µg/ml, F: 200 µg/ml) exhibit a clear correlation with a reduction in cell count, providing valuable insights into the potential cytotoxic effects and dose-response relationship of Han: Eu^{3+} NCs on MCF7 breast cancer cell lines. The presented results in Table 7 showed the effect of various culture conditions on cell viability and the IC50 concentration of Han: Eu^{3+} NCs. The cells were subjected to different culture conditions, including untreated, doxorubicin-1 µM/ml, and different concentrations of Han: Eu^{3+} NCs. After the incubation period, the percentage of cell viability was calculated for each condition. The untreated cells showed 100 % cell viability, while doxorubicin-1 µM/ml resulted in a 51.64 % cell viability, indicating the cytotoxic effects of the drug on the cells. Treatment with Han: Eu^{3+} NCs at different concentrations resulted in different levels of cell viability, with the lowest concentration tested (6.25 µg/ml) showing a high percentage of viability (92.83 %). However, as the concentration of Han: Eu^{3+} NCs increased, the percentage of cell viability decreased, indicating a dose-dependent cytotoxic effect of Han: Eu^{3+} NCs on the cells. The IC50 concentration for Han: Eu^{3+} NCs was found to be 54.43 µg/ml, indicating that this concentration was required to inhibit cell growth by 50 %. At the highest concentration of Han: Eu^{3+} NCs tested (200 µg/ml), 12.51 % of cells remained viable, suggesting a strong cytotoxic effect of this concentration on the cells. Overall, the results suggested that Han: Eu^{3+} NCs had a dose-dependent cytotoxic effect on the cells, with higher concentrations resulting in lower cell viability, and that the IC50 concentration of Han: Eu^{3+} NCs was 54.43 µg/ml.

3.10.2. Europium doped hydroxyapatite nanocomposites of 4T1 cell lines

Fig. 13(a–f) and 14 demonstrates a dose-dependent analysis, revealing a discernible decrease in the number of cells as the concentration of Han: Eu^{3+} NCs increases. The concentrations examined (A: 6.25 µg/ml, B: 12.5 µg/ml, C: 25 µg/ml, D: 50 µg/ml, E: 100 µg/ml, F: 200 µg/ml) exhibit a clear correlation with a reduction in cell count, providing valuable insights into the potential cytotoxic effects and dose-response relationship of Han: Eu^{3+} NCs on 4T1 breast cancer cell lines. Table 8 provides information on the effect of various culture conditions on cell viability and IC50 concentration in 4T1 cell lines treated with Han: Eu^{3+} NCs. Untreated cells show 100 % viability, while treatment with 1 µM Dox (a chemotherapy drug) reduces cell viability to 46.25 %. Treatment with different

Table 6
Details of drug treatment to respective cell lines used for the study.

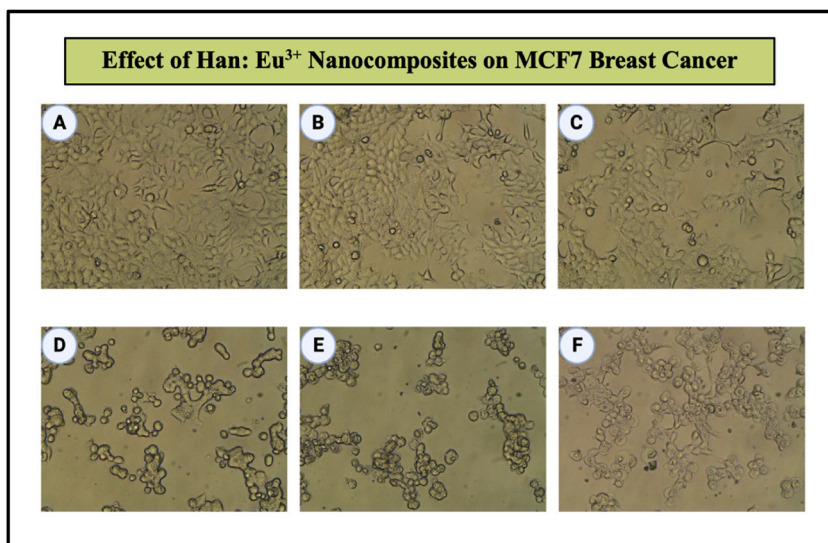| S.No	Culture condition	Cell line	Concentrations treated to cells
1	Untreated	MCF7	No treatment
2	Blank	–	Only Media without cells
3	Doxorubicin	MCF7	1uM/mL
4	Han: Eu^{3+} NCs	MCF7	6 (6.25, 12.5, 25, 50, 100, 200 µg/ml)
3	Han: Eu^{3+} NCs	4T1	6 (6.25,12.5, 25, 50, 100, 200 µg/ml)

Fig. 11. The image depicts a series of drug concentration experiment conducted on MCF7 Breast cancer cell lines. The experiment aims to investigate the effect of varying concentrations (A:6.25 µg/ml, B:12.5 µg/ml, C:25 µg/ml, D:50 µg/ml, E:100 µg/ml, F:200 µg/ml) of Han: Eu^{3+} NCs, on the MCF7 Breast Cancer cell lines, which serve as a representative model for studying breast cancer.
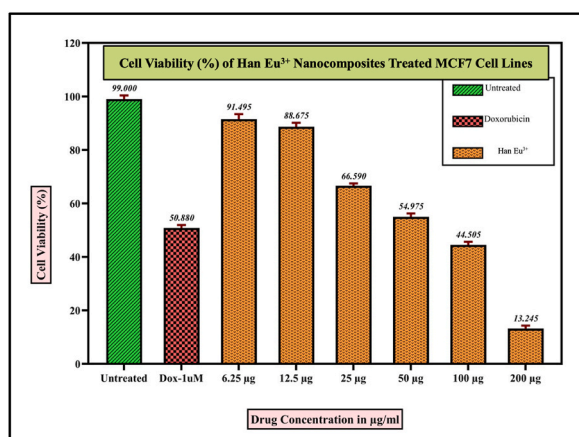

Fig. 12. Percentage of Cell viability values of Han: Eu^{3+} NCs treated MCF7 cells after the incubation period of 24hrs.

Table 7
Percentage of cell viability values of Han: Eu^{3+} NCs effect on MCF7 cells after the treatment period of 24hrs.

Culture condition	Percentage of Cell viability	IC50 conc (µg/ml)
Untreated	100	IC50 conc=54.43 µg/ml
Doxorubicin- 1 µM/ml	51.64	
Han: Eu^{3+} NCs -6.25 µg	92.83	
Han: Eu^{3+} NCs -12.5 µg	89.72	
Han: Eu^{3+} NCs -25 µg	65.95	
Han: Eu^{3+} NCs -50 µg	54.08	
Han: Eu^{3+} NCs -100 µg	43.69	
Han: Eu^{3+} NCs -200 µg	12.51	

concentrations of Han: Eu^{3+} NCs results in varying degrees of cell death. As the concentration of Han: Eu^{3+} NCs increases from 6.25 to 200 µg/mL, the viability of cells decreases from 90.16 % to 34.97 %. The IC50 concentration of Han: Eu^{3+} NCs for the 4T1 cell line cannot be directly determined from the data presented. However, it is expected to be higher than 50 µg/mL based on the viability data. A higher viability percentage indicates a higher IC50 concentration, meaning that the substance is less effective at inhibiting cell growth at a higher concentration.
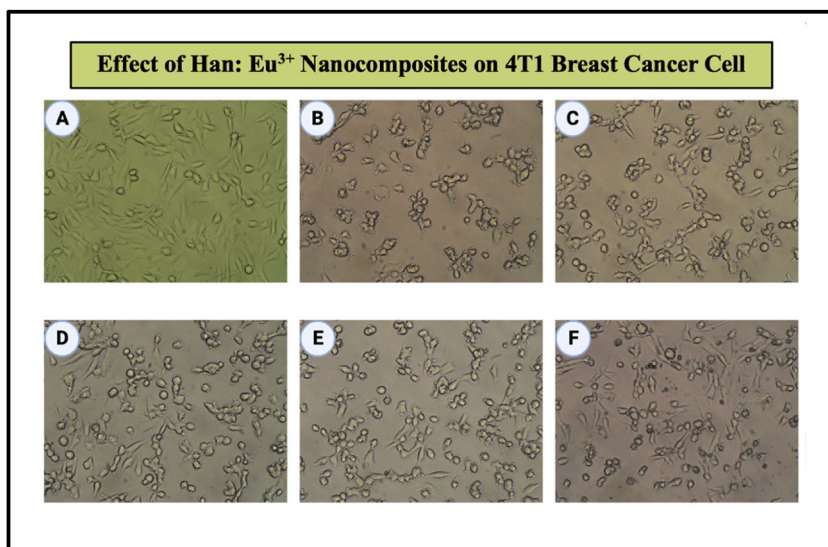
Fig. 13. The image depicts a series of drug concentration experiments conducted on 4T1 Breast cancer cell lines. The experiment aim to investigate the effect of varying concentrations (A:6.25 µg/ml, B:12.5 µg/ml, C:25 µg/ml, D:50 µg/ml, E:100 µg/ml, F:200 µg/ml) of Han: Eu^{3+} NCs, on the 4T1 Breast Cancer cell lines, which serve as a representative model for studying breast cancer.
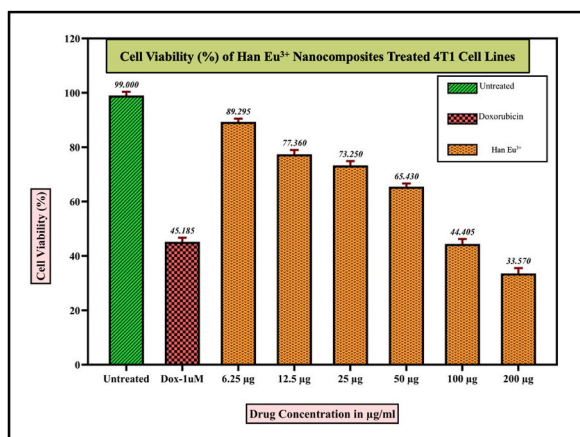

Fig. 14. Cell viability (%) values of Han: Eu^{3+} NCs treated 4T1 cells after the incubation period of 24hrs.

Table 8

Percentage of cell viability values of Han: Eu^{3+} NCs effect on 4T1 cells after the treatment period of 24hrs.

Culture condition	Cell viability (%)	IC50 conc (µg/ml)
Untreated	100	87.32 µg/ml
Dox-1 uM	46.25	
Han: Eu^{3+} NCs -6.25 µg	90.16	
Han: Eu^{3+} NCs -12.5 µg	76.23	
Han: Eu^{3+} NCs -25 µg	72.18	
Han: Eu^{3+} NCs -50 µg	64.57	
Han: Eu^{3+} NCs -100 µg	45.69	
Han: Eu^{3+} NCs -200 µg	34.97	

Furthermore, Han: Eu^{3+} NCs exhibits several key advantages for its application in MCF7 and 4T1 Breast Cancer Cell Lines. It is biocompatible, making it a safe choice for medical use, and its luminescent properties are excellent for imaging and diagnostics [57]. The material's multifaceted surface composition enables effective interaction with cancer cells, potentially enabling targeted drug delivery and reducing off-target effects [58]. Additionally, it demonstrates cytotoxic properties against MCF7 breast cancer cells, suggesting therapeutic potential. Its use of hydroxyapatite, a well-established material, can streamline regulatory approval and clinical

translation, and its biodegradability minimizes long-term accumulation concerns. These attributes position Han: Eu^{3+} NCs as a promising candidate for breast cancer diagnosis and treatment in the field of cancer research and therapy.

4. Conclusion

This investigation explores the potential of hydroxyapatite nanocomposite doped with Eu^{3+} ions (Han: Eu^{3+} NCs) for breast cancer management, specifically targeting MCF7 and 4T1 cell lines. These nanocomposites were successfully synthesized with a focus on achieving luminescence and biocompatibility. Key findings include their crystalline structure (25 nm) and multifaceted surface composition. The optical characteristics of Han: Eu^{3+} NCs, particularly their excitation and emission spectra, reveal their potential in cancer diagnostics and imaging. Notably, they emit red radiation when exposed to UV light, making them promising for identifying cancerous tumors within the human body. Furthermore, we conducted cytotoxicity assessments, demonstrating the cytotoxic properties of Han: Eu^{3+} NCs on MCF7 breast cancer cells, with an established IC50 concentration. This suggests their potential as a therapeutic alternative for breast cancer. Our study provides an overview of the synthesis, characterization, luminescent properties, and cytotoxicity of these nanocomposites, supporting their prospective use in focused therapeutic interventions for breast carcinoma. Nevertheless, further research and *in vivo* experiments are needed to determine their effectiveness and safety in breast cancer treatment.

Data availability statement

There was no utilization of data for the research described in the article.

CRediT authorship contribution statement

K Sai Manogna: Writing – original draft, Methodology, Data curation. **B. Deva Prasad Raju:** Writing – review & editing, Supervision, Formal analysis, Conceptualization. **G. Rajasekhara Reddy:** Data curation. **Parashuram Kallem:** Funding acquisition. **Mannur Ismail Shaik:** Funding acquisition. **N. John Sushma:** Writing – review & editing, Validation, Formal analysis, Conceptualization.

Declaration of competing interest

The authors confirm that there are no recognized financial conflicts or personal connections that could potentially impact the integrity of the work presented in this paper.

List of Abbreviations

Eu^{3+}	Europium
HA	Hydroxyapatite
Han	Hydroxyapatite nanocomposites
Han	Eu^{3+} NCs: Europium doped Hydroxyapatite nanocomposites
EPR	Enhanced Permeation and Retention
COX-2	Cyclooxygenase 2
FU	Fluorouracil
RAS/ERK Pathway	Mitogen activated protein kinase/Extracellular signal regulated Kinase Pathway
NF-κB	Nuclear Factor kappa B Pathway
AMPK	AMP – activated Protein Kinase Pathway
TAM	Tamoxifen
ER	Estrogen/Oestrogen Receptor
DOX	Doxorubicin
ROS	Reactive Oxygen Species
PLD	PEGylated Liposomal Doxorubicin
Ca	Calcium
Cl	Chlorine
P	Phosphorous
Na	Sodium

XRD	X-Ray Diffraction Spectroscopy
XPS	X-ray Photoelectron Spectroscopy
DSC	Differential Scanning Calorimetry
FTIR	Fourier Transform Infrared Spectroscopy
SEM	Scanning Electron Microscopy
SEM – EDS	Scanning Electron Microscopy - Energy Dispersive X-Ray Spectroscopy
PL	Photoluminescence studies
MTT Assay	3-[4,5-dimethylthiazol-2-yl]-2,5 diphenyl tetrazolium bromide Assay
IC50	Half – Maximal Inhibitory Concentration

References

[1] Uma Prabhakar, Hiroshi Maeda, Rakesh K. Jain, M. Eva, Sevick-Muraca, William Zamboni, Omid C. Farokhzad, Simon T. Barry, Alberto Gabizon, Piotr Grodzinski, David C. Blakey, Challenges and Key Considerations of the Enhanced Permeability and Retention Effect for Nanomedicine Drug Delivery in Oncology, 2013, pp. 2412–2417, https://doi.org/10.1158/0008-5472.CAN-12-4561.

[2] U.I.C.C. Breast Cancer, Global cancer control reports. https://www.uicc.org/what-we-do/areas-focus/breast-cancer, 2023. (Accessed 3 August 2023).

[3] Horner MJ., SEER cancer statistics review, 1975-2006. http://seer.cancer.gov/csr/1975_2006/.2009.

[4] Ahmedin Jemal, Freddie Bray, Melissa M. Center, Jacques Ferlay, Elizabeth Ward, David Forman, Global cancer statistics, CA A Cancer J. Clin. 61 (No. 2) (2011) 69–90, https://doi.org/10.3322/caac.20107.

[5] Scott Valastyan, Robert A. Weinberg, Tumor metastasis: molecular insights and evolving paradigms, Cell 147 (No. 2) (2011) 275–292, https://doi.org/10.1016/j.cell.2011.09.024.

[6] Elly Harris, Mitchel Barry, Malcolm R. Kell, Meta-analysis to determine if surgical resection of the primary tumour in the setting of stage IV breast cancer impacts on survival, Ann. Surg Oncol. 20 (2013) 2828–2834, https://doi.org/10.1245/s10434-013-2998-2.

[7] Michael M. Gottesman, Orit Lavi, Matthew D. Hall, Jean-Pierre Gillet, Toward a better understanding of the complexity of cancer drug resistance, Annu. Rev. Pharmacol. Toxicol. 56 (2016) 85–102, https://doi.org/10.1146/annurev-pharmtox-010715-103111.

[8] Marcus Schmidt, Dose-dense chemotherapy in metastatic breast cancer: shortening the time interval for a better therapeutic index, Breast Care 11 (No. 1) (2016) 22–26, https://doi.org/10.1159/000442726.

[9] Yiwen Dong, Tianzhu Yu, Ling Ding, Erik Laurini, Yuanyu Huang, Mengjie Zhang, Yuhua Weng, et al., A dual targeting dendrimer-mediated siRNA delivery system for effective gene silencing in cancer therapy, J. Am. Chem. Soc. 140 (No. 47) (2018) 16264–16274, https://doi.org/10.1021/jacs.8b10021.

[10] Dinesh Dhumal, Wenjun Lan, Ling Ding, Yifan Jiang, Zhenbin Lyu, Erik Laurini, Domenico Marson, et al., An ionizable supramolecular dendrimer nanosystem for effective siRNA delivery with a favorable safety profile, Nano Res. 14 (2021) 2247–2254, https://doi.org/10.1007/s12274-020-3216-8.

[11] Sudeep Pushpakom, Francesco Iorio, Patrick A. Eyers, K. Jane Escott, Shirley Hopper, Andrew Wells, Andrew Doig et al. "Drug repurposing: progress, challenges and recommendations, Nat. Rev. Drug Discov. 18 (No. 1) (2019) 41–58, https://doi.org/10.1038/nrd.2018.168.

[12] Home - ClinicalTrials.gov, (n.d.). ⟨https://clinicaltrials.gov/. (Accessed 3 August, 2023).

[13] Jennifer M. Curry, Dahlia M. Besmer, Timothy K. Erick, Nury Steuerwald, Lopamudra Das Roy, Priyanka Grover, Shanti Rao, et al., Indomethacin enhances anti-tumor efficacy of a MUC1 peptide vaccine against breast cancer in MUC1 transgenic mice, PLoS One 14 (No. 11) (2019) e0224309, https://doi.org/10.1371/journal.pone.0224309.

[14] Jieqing Li, Hao Qiongyu, Wei Cao, Jaydutt V. Vadgama, Yong Wu, Celecoxib in Breast Cancer Prevention and Therapy, Cancer Management and Research, 2018, pp. 4653–4667, https://doi.org/10.2147/CMAR.S178567.

[15] Chen Chen, Hui Ling Shen, Jing Yang, Yun Chen Qiao, Lin Xu Wen, Preventing chemoresistance of human breast cancer cell line, MCF-7 with celecoxib, J. Cancer Res. Clin. Oncol. 137 (2011) 9–17, https://doi.org/10.1007/s00432-010-0854-3.

[16] Fatemeh Kalalinia, Fatemeh Elahian, Javad Behravan, Potential role of cyclooxygenase-2 on the regulation of the drug efflux transporter ABCG2 in breast cancer cell lines, J. Cancer Res. Clin. Oncol. 137 (2011) 321–330, https://doi.org/10.1007/s00432-010-0893-9.

[17] Matteo Parri, Paola Chiarugi, Rac and Rho GTPases in cancer cell motility control, Cell Commun. Signal. 8 (2010) 1–14, https://doi.org/10.1186/1478-811X-8-23.

[18] Entezar-Almahdi, Soliman Mohammadi-Samani Elaheh, Lobat Tayebi, Fatemeh Farjadian, Recent advances in designing 5-fluorouracil delivery systems: a stepping stone in the safe treatment of colorectal cancer, Int. J. Nanomed. (2020) 5445–5458, https://doi.org/10.2147/IJN.S257700.

[19] Chinmayee Sethy, Chanakya Nath Kundu, 5-Fluorouracil (5-FU) resistance and the new strategy to enhance the sensitivity against cancer: Implication of DNA repair inhibition, Biomed. Pharmacother. 137 (2021) 111285, https://doi.org/10.1016/j.biopha.2021.111285.

[20] Liliana-Roxana Balahura, Sorina Dinescu, Mihaela Balaş, Alexandra Cernencu, Adriana Lungu, George Mihail Vlăsceanu, Horia Iovu, Marieta Costache, Cellulose nanofiber-based hydrogels embedding 5-FU promote pyroptosis activation in breast cancer cells and support human adipose-derived stem cell proliferation, opening new perspectives for breast tissue engineering, Pharmaceutics 13 (No. 8) (2021) 1189, https://doi.org/10.3390/pharmaceutics13081189.

[21] Takayuki Watanabe, Takaaki Oba, Keiji Tanimoto, Tomohiro Shibata, Shinobu Kamijo, Ken-ichi Ito, Tamoxifen resistance alters sensitivity to 5-fluorouracil in a subset of estrogen receptor-positive breast cancer, PLoS One 16 (No. 6) (2021) e0252822, https://doi.org/10.1371/journal.pone.0252822.

[22] Reema S. Wahdan-Alaswad, Ann D. Thor, Metformin activity against breast cancer: mechanistic differences by molecular subtype and metabolic conditions, in: Metformin, IntechOpen, London, UK, 2020.

[23] J. Faria, G. Negalha, A. Azevedo, F. Martel, Metformin and breast cancer: molecular targets, J. Mammary Gland Biol. Neoplasia 24 (2019) 111–123, https://doi.org/10.1007/s10911-019-09429-z.

[24] Jiyoung Lee, Ali E. Yesilkanal, Joseph P. Wynne, Frankenberger Casey, Juan Liu, Jielin Yan, Mohamad Elbaz, et al., Effective breast cancer combination therapy targeting BACH1 and mitochondrial metabolism, Nature 568 (No. 7751) (2019) 254–258, https://doi.org/10.1038/s41586-019-1005-x.

[25] Bin Shi, Xinyu Hu, Huimin He, Wenzheng Fang, Metformin suppresses breast cancer growth via inhibition of cyclooxygenase-2, Oncol. Lett. 22 (No. 2) (2021) 1–14, https://doi.org/10.3892/ol.2021.12876.

[26] Zhe Zhang, Li Zhou, Na Xie, Edouard C. Nice, Tao Zhang, Yongping Cui, Canhua Huang, Overcoming cancer therapeutic bottleneck by drug repurposing, Signal Transduct. Targeted Ther. 5 (No. 1) (2020) 113, https://doi.org/10.1038/s41392-020-00213-8.

[27] Yuan Gao, Qingyao Shang, Wenyu Li, Wenxuan Guo, Stojadinovic Alexander, Ciaran Mannion, Yan-gao Man, Tingtao Chen, Antibiotics for cancer treatment: a double-edged sword, J. Cancer 11 (No. 17) (2020) 5135.

[28] Jelena Lazovic, Lea Guo, Jonathan Nakashima, Leili Mirsadraei, William Yong, Hyun J. Kim, Benjamin Ellingson, Hong Wu, Whitney B. Pope, Nitroxoline induces apoptosis and slows glioma growth in vivo, Neuro Oncol. 17 (No. 1) (2015) 53–62, https://doi.org/10.1093/neuonc/nou139.

[29] Nguyen Minh Tuan, Hoon Lee Chang, Penfluridol as a candidate of drug repurposing for anticancer agent, Molecules 24 (No. 20) (2019) 3659, https://doi.org/10.3390/molecules24203659.

[30] Nehal Gupta, Parul Gupta, Sanjay K. Srivastava, Penfluridol overcomes paclitaxel resistance in metastatic breast cancer, Sci. Rep. 9 (No. 1) (2019) 5066, https://doi.org/10.1038/s41598-019-41632-0.

[31] Marco Varalda, Annamaria Antona, Valentina Bettio, Konkonika Roy, Ajay Vachamaram, Vaibhav Yellenki, Alberto Massarotti, Gianluca Baldanzi, Daniela Capello, Psychotropic drugs show anticancer activity by disrupting mitochondrial and lysosomal function, Front. Oncol. 10 (2020) 562196, https://doi.org/10.3389/fonc.2020.562196.

[32] Suyash Srivastava, Fatema Tuz Zahra, Nehal Gupta, Paul E. Tullar, Sanjay K. Srivastava, Constantinos M. Mikelis, Low dose of penfluridol inhibits VEGF-induced angiogenesis, Int. J. Mol. Sci. 21 (No. 3) (2020) 755, https://doi.org/10.3390/ijms21030755.

[33] Jingwei Yao, Kun Deng, Jialu Huang, Ruimin Zeng, Jianhong Zuo, Progress in the understanding of the mechanism of tamoxifen resistance in breast cancer, Front. Pharmacol. 11 (2020) 592912, https://doi.org/10.3389/fphar.2020.592912.

[34] Holm Eggemann, Cosima Brucker, Michael Schrauder, Marc Thill, Felix Flock, Mattea Reinisch, Serban-Dan Costa, Atanas Ignatov, Survival benefit of tamoxifen in male breast cancer: prospective cohort analysis, Br. J. Cancer 123 (No. 1) (2020) 33–37, https://doi.org/10.1038/s41416-020-0857-z.

[35] Huma Dar, Annelie Johansson, Nordenskjöld Anna, Adina Iftimi, Christina Yau, Gizeh Perez-Tenorio, Christopher Benz, et al., Assessment of 25-year survival of women with estrogen receptor–positive/ERBB2-negative breast cancer treated with and without tamoxifen therapy: a secondary analysis of data from the Stockholm tamoxifen randomized clinical trial, JAMA Netw. Open 4 (No. 6) (2021) http://jamanetwork.com/article.aspx?doi=10.1001/jamanetworkopen.2021.14904.

[36] Mikael Eriksson, Martin Eklund, Signe Borgquist, Roxanna Hellgren, Sara Margolin, Linda Thoren, Ann Rosendahl, et al., Low-dose tamoxifen for mammographic density reduction: a randomized controlled trial, J. Clin. Oncol. 39 (No. 17) (2021) 1899.

[37] Mohammad Taheri, Bashdar Mahmud Hussen, Farhad Tondro Anamag, Hamed Shoorei, Marcel E. Dinger, Soudeh Ghafouri-Fard, The role of miRNAs and lncRNAs in conferring resistance to doxorubicin, J. Drug Target. 30 (No. 1) (2022) 1–21, https://doi.org/10.1080/1061186X.2021.1909052.

[38] Salah Mabrouk Khallaf, Jasmine Roshdy, Abeer Ibrahim, Pegylated liposomal doxorubicin in patients with metastatic triple-negative breast cancer: 8-year experience of a single center, J. Egypt. Natl. Cancer Inst. 32 (2020) 1–10, https://doi.org/10.1186/s43046-020-00034-4.

[39] Eriko Katsuta, Li Yan, Masayuki Nagahashi, Raza Ali, Jamie L. Sturgill, Debra E. Lyon, Omar M. Rashid, Nitai C. Hait, Kazuaki Takabe, Doxorubicin effect is enhanced by sphingosine-1-phosphate signaling antagonist in breast cancer, J. Surg. Res. 219 (2017) 202–213, https://doi.org/10.1016/j.jss.2017.05.101.

[40] Varun KA. Sreenivasan, Andrei V. Zvyagin, Ewa M. Goldys, Luminescent nanoparticles and their applications in the life sciences, J. Phys. Condens. Matter 25 (No. 19) (2013) 194101, https://doi.org/10.1088/0953-8984/25/19/194101.

[41] Yi-Cheun Yeh, Brian Creran, Vincent M. Rotello, Gold nanoparticles: preparation, properties, and applications in bionanotechnology, Nanoscale 4 (No. 6) (2012) 1871–1880, https://doi.org/10.1039/C1NR11188D.

[42] K. David Wegner, Niko Hildebrandt, Quantum dots: bright and versatile in vitro and in vivo fluorescence imaging biosensors, Chem. Soc. Rev. 44 (No. 14) (2015) 4792–4834, https://doi.org/10.1039/C4CS00532E.

[43] Francesca Oltolina, Luca Gregoletto, Donato Colangelo, Jaime Gomez-Morales, José Manuel Delgado-López, Maria Prat, Monoclonal antibody-targeted fluorescein-5-isothiocyanate-labeled biomimetic nanoapatites: a promising fluorescent probe for imaging applications, Langmuir 31 (No. 5) (2015) 1766–1775, https://doi.org/10.1021/la503747s.

[44] S.R. Hemelaar, P. De Boer, M. Chipaux, W. Zuidema, T. Hamoh, F. Perona Martinez, A. Nagl, J.P. Hoogenboom, B.N.G. Giepmans, R. Schirhagl, Nanodiamonds as multi-purpose labels for microscopy, Sci. Rep. 7 (No. 1) (2017) 720, https://doi.org/10.1038/s41598-017-00797-2.

[45] Sing Muk Ng, Masilamany Koneswaran, Ramaier Narayanaswamy, A review on fluorescent inorganic nanoparticles for optical sensing applications, RSC Adv. 6 (No. 26) (2016) 21624–21661, https://doi.org/10.1039/C5RA24987B.

[46] Ahmed Al-Kattan, Sophie Girod-Fullana, Cédric Charvillat, Hélène Ternet-Fontebasso, Pascal Dufour, Jeannette Dexpert-Ghys, Véronique Santran, et al., Biomimetic nanocrystalline apatites: emerging perspectives in cancer diagnosis and treatment, Int. J. Pharm. 423 (No. 1) (2012) 26–36, https://doi.org/10.1016/j.ijpharm.2011.07.005.

[47] Sutapa Roy Ramanan, Ramanan Venkatesh, A study of hydroxyapatite fibers prepared via sol–gel route, Mater. Lett. 58 (No. 26) (2004) 3320–3323, https://doi.org/10.1016/j.matlet.2004.06.030.

[48] Nooshin Kashi, Mahdi Momeni, Habib Hamidinezhad, Biological characterization of the zinc-modified hydroxyapatite coated by a pulsed laser deposition method, Phys. Scripta 97 (No. 8) (2022) 085709, https://doi.org/10.1088/1402-4896/ac82cf.

[49] Jayachandran Venkatesan, Se-Kwon Kim, Nano-hydroxyapatite composite biomaterials for bone tissue engineering—a review, J. Biomed. Nanotechnol. 10 (No. 10) (2014) 3124–3140, https://doi.org/10.1166/jbn.2014.1893.

[50] Jason M. Millward, Angela Ariza de Schellenberger, Dominique Berndt, Laura Hanke-Vela, Eyk Schellenberger, Sonia Waiczies, Matthias Taupitz, Yuske Kobayashi, Susanne Wagner, Carmen Infante-Duarte, Application of europium-doped very small iron oxide nanoparticles to visualize neuroinflammation with MRI and fluorescence microscopy, Neuroscience 403 (2019) 136–144, https://doi.org/10.1016/j.neuroscience.2017.12.014.

[51] Afanasy V. Lunin, Ilya L. Sokolov, Ivan V. Zelepukin, Ilya V. Zubarev, Maria N. Yakovtseva, Elizaveta N. Mochalova, Julian M. Rozenberg, Maxim P. Nikitin, Eugene L. Kolychev, Spindle-like MRI-active europium-doped iron oxide nanoparticles with shape-induced cytotoxicity from simple and facile ferrihydrite crystallization procedure, RSC Adv. 10 (No. 12) (2020) 7301–7312, https://doi.org/10.1039/C9RA10683A.

[52] Binbin Zhang, Xuelin Dong, Zhou Qi, Shan Lu, Xinwei Zhang, Yonggui Liao, Yajiang Yang, Hong Wang, Carboxymethyl chitosan–promoted luminescence of lanthanide metallogel and its application in assay of multiple metal ions, Carbohydr. Polym. 263 (2021) 117986, https://doi.org/10.1016/j.carbpol.2021.117986.

[53] Koen Binnemans, Interpretation of europium (III) spectra, Coord. Chem. Rev. 295 (2015) 1–45, https://doi.org/10.1016/j.ccr.2015.02.015.

[54] F.W. Jr. Billmeyer, M. Saltzman, Principles of Color Technology, John Wiley and Sons, 1981.

[55] Nisha Deopa, Babloo Kumar, Mukesh K. Sahu, P. Rekha Rani, A.S. Rao, Effect of Sm^{3+} ions concentration on borosilicate glasses for reddish orange luminescent device applications, J. Non-Cryst. Solids 513 (2019) 152–158, https://doi.org/10.1016/j.jnoncrysol.2019.03.025.

[56] R. Cao, C. Chen, F. Cheng, T. Chen, B. Lan, L. Li, R. Liu, J. Wang, Synthesis and luminescence properties of Eu3+, Dy3+ co-doped Ca3Bi (PO4) 3 single-phase phosphor, J. Lumin. 257 (2023) 119731.

[57] Yunfei Xie, Wangmei He, Fang Li, Thalagalage Shalika Harshani Perera, Lin Gan, Yingchao Han, Xinyu Wang, Shipu Li, Honglian Dai, Luminescence enhanced Eu3+/Gd3+ co-doped hydroxyapatite nanocrystals as imaging agents in vitro and in vivo, ACS Appl. Mater. Interfaces 8 (16) (2016) 10212–10219.

[58] Fakhar Ud Din, Waqar Aman, Izhar Ullah, Omer Salman Qureshi, Omer Mustapha, Shumaila Shafique, Zeb Alam, Effective use of nanocarriers as drug delivery systems for the treatment of selected tumors, Int. J. Nanomed. (2017) 7291–7309.

[59] M. Baira, A. Bekhti-Siad, K. Hebali, H. Bouhani-Benziane, M. Sahnoun, Charge compensation mechanisms in favor of the incorporation of the Eu3+ ion into the ZnO host lattice, Phys. B Condens. Matter 537 (2018) 296–300.